Metrologia

Determination of the Boltzmann constant with cylindrical acoustic gas thermometry: new and previous results combined

IOP Publishing | Bureau International des Poids et Mesures Metrologia

Metrologia **54** (2017) 748–762 https://doi.org/10.1088/1681-7575/aa7b4a

Determination of the Boltzmann constant with cylindrical acoustic gas thermometry: new and previous results combined

X J Feng[1], J T Zhang[1], H Lin[1], K A Gillis[2], J B Mehl[3], M R Moldover[2], K Zhang[1] and Y N Duan[1]

[1] National Institute of Metrology, Beijing 100029, People's Republic of China
[2] National Institute of Standards and Technology, Gaithersburg, MD 20899-8360, United States of America
[3] 36 Zunuqua Trail, PO Box 307, Orcas, WA 98280-0307, United States of America

E-mail: zhangjint@nim.ac.cn

Received 22 May 2017, revised 22 June 2017
Accepted for publication 23 June 2017
Published 11 September 2017

Abstract

We report a new determination of the Boltzmann constant k_B using a cylindrical acoustic gas thermometer. We determined the length of the copper cavity from measurements of its microwave resonance frequencies. This contrasts with our previous work (Zhang *et al* 2011 *Int. J. Thermophys.* **32** 1297, Lin *et al* 2013 *Metrologia* **50** 417, Feng *et al* 2015 *Metrologia* **52** S343) that determined the length of a different cavity using two-color optical interferometry. In this new study, the half-widths of the acoustic resonances are closer to their theoretical values than in our previous work. Despite significant changes in resonator design and the way in which the cylinder length is determined, the value of k_B is substantially unchanged. We combined this result with our four previous results to calculate a global weighted mean of our k_B determinations. The calculation follows CODATA's method (Mohr and Taylor 2000 *Rev. Mod. Phys*. **72** 351) for obtaining the weighted mean value of k_B that accounts for the correlations among the measured quantities in this work and in our four previous determinations of k_B. The weighted mean $\hat{\boldsymbol{k}}_B$ is $1.380\,6484(28) \times 10^{-23}$ J K^{-1} with the relative standard uncertainty of 2.0×10^{-6}. The corresponding value of the universal gas constant is 8.314 459(17) J K^{-1} mol^{-1} with the relative standard uncertainty of 2.0×10^{-6}.

Keywords: Boltzmann constant, cylindrical acoustic gas thermometry, acoustic resonance, microwave resonance

(Some figures may appear in colour only in the online journal)

1. Introduction

The planned redefinition of four base SI units in terms of fundamental constants is a milestone in the history of the global metrology community. As a part of this event, the kelvin will be defined by fixing the Boltzmann constant k_B [1–4]. Re-determining k_B with state-of-the-art uncertainty is a precondition for the redefinition of the kelvin. Several primary thermometry methods have been applied to this re-determination [5]. Among these methods, acoustic gas thermometry (AGT) has contributed the largest weight to the re-determination of the Boltzmann constant [6–11].

For an ideal gas composed of molecules of mass m in thermal equilibrium, the thermodynamic temperature T measures the average kinetic energy of a molecule: $(1/2)\,mv_{RMS}^2 = (3/2)k_BT$, where v_{RMS} is the root-mean-square (RMS) velocity of the molecule. The kinetic energy is related to the speed of sound w_0 and the heat capacity ratio γ_0, of the ideal gas by $v_{RMS}^2 = (3/\gamma_0)w_0^2$. For a monatomic gas, the heat capacity ratio γ_0 is exactly 5/3. The AGT accurately measures

the speed of sound $w(p)$ of a real monatomic gas as a function of the pressure on an isotherm and obtains w_0 using the acoustic virial expansion of $w^2(p)$ [12]. The Boltzmann constant k_B is then obtained by:

$$k_B = \frac{w_0^2 M}{T\gamma_0 N_A} \tag{1}$$

where M is the average molar mass of the gas; N_A is the Avogadro constant, which is known with the relative standard uncertainty[4] $u_r(N_A) = 1.2 \times 10^{-8}$ [6].

The state-of-the-art AGT obtains the speed of sound by measuring acoustic resonance frequencies of specific modes of a cavity with known dimensions. Both spherical and cylindrical cavities have been used for this purpose. The National Institute of Metrology in China (NIM) has been collaborating with the National Institute of Standards and Technology (NIST) to refine the determination of k_B using cylindrical acoustic gas thermometry, c-AGT [11, 13, 14]. As part of this effort, we have tested many fixed-path-length cylindrical cavities. Initially, our cavities were enclosed by bearing-steel cylindrical shells and transparent fused-silica endplates. These endplates allowed us to accurately measure the lengths of the cavities using two-color laser interferometry. However, this design had two disadvantages: (1) The fabrication of ports and seals in the endplates was complex; the fused-silica endplates were particularly difficult to modify after they were fabricated. (2) We encountered temperature-dependent problems with seals because the thermal expansion of silica is much smaller than that of the bearing steel. To avoid these problems, we recently [15] started using cylindrical cavities enclosed by copper cylindrical shells and copper endplates. These cavities allowed us to determine their lengths L and radii a using microwave resonances [16, 17]. The microwave approach to measuring L and a has been used in many contexts to determine the dimensions of metal-walled cavities [18–20], including those made of ferromagnetic metals [21]. A recent microwave determination of the average radius of a copper-walled, quasi-spherical cavity had the remarkably-small relative uncertainty $u_r(a) = 0.19 \times 10^{-6}$ [8].

The present work differs from our previous work [11, 13, 14] in three ways. First, we replaced the steel cavity with the copper cavity. Second, we replaced the laser interferometry with the microwave measurements of the cavity's length. Third, we continuously flowed the sample gas through the cylindrical cavity instead of filling the cavity to a maximum pressure before measuring the speed of sound $w(p)$ on each isotherm. Here, we report the re-determination of k_B using these three improvements of c-AGT.

Because of the significant changes in the resonator's design and the way in which the cavity's length was determined, our present result is, in many ways, independent of our previous results. Therefore, we combined the present result with our four previous results to produce a global weighted mean $\hat{k}_B$ of our determinations of k_B that used c-AGT. To determine $\hat{k}_B$ we applied the CODATA-recommended approach [22, 23] to account for the correlations among the measured quantities.

[4] Unless otherwise stated, all uncertainties are one standard uncertainty corresponding to a 68% confidence level.

2. Fundamentals of the measurement

The principles of using c-AGT for determining k_B have been described in detail in our previous publications [11, 13, 14]. Here, we summarize the key points of deducing the length L from microwave resonance frequencies and of determining the ideal-gas speed of sound in argon from acoustic resonant frequencies.

We consider an ideal right circular cylindrical cavity enclosed by perfectly-conducting, non-magnetic surfaces. The resonance frequencies of the transverse magnetic (TM) microwave modes of the cavity are:

$$\left(f^0_{spq}\right)_{TM} = \frac{c_0}{2\pi n}\sqrt{\left(\frac{s\pi}{L}\right)^2 + \left(\frac{\chi_{pq}}{a}\right)^2}, \tag{2}$$

where $c_0 = 299\,792\,458$ m·s^{-1} is the defined speed of light in vacuum; f^0 is an unperturbed resonant frequency of this ideal cavity; n is the refractive index of the gas in the cavity; the subscript TM indicates that the mode is TM, and the subscripts $s = 0, 1, 2\ldots$; $p = 0, \pm1, \pm2\ldots$; and $q = 1, 2, 3\ldots$ index the variations of the electromagnetic field vectors along the axial, angular, and radial directions, respectively. The eigenvalue χ_{pq} is the qth root of $J_p(\chi) = 0$ and J_p is the Bessel function of order p. The TM modes with $p = 0$ are non-degenerate. Thus, the modes $(s0q)_{TM}$ are suitable for determining L and a of the cylindrical cavity. We excited and detected these modes using straight probe antennas which are easy to fabricate and install [15]. We deduced L from the four ideal frequencies $(f^0_{1,0,1})_{TM}$, $(f^0_{2,0,1})_{TM}$, $(f^0_{3,0,1})_{TM}$, $(f^0_{4,0,1})_{TM}$ by fitting a straight line to four coordinate pairs (x_i, y_i) defined by $x_i \equiv (s\pi)^2$ and $y_i \equiv (2\pi n f^0/c_0)^2$. The slope (d$y$/d$x$) of the fitted line is related to L by:

$$L = \frac{1}{\sqrt{\mathrm{d}y/\mathrm{d}x}}. \tag{3}$$

For determining the speed of sound, we used the non-degenerate longitudinal acoustic modes $(l00)$ of the gas in the cylindrical cavity. The speed of sound is related to the ideal frequencies of the $(l00)$ modes by

$$f^0_l = \frac{lw}{2L} \tag{4}$$

where $l = 1, 2,\ldots$ is the index (and also the eigenvalue) of the longitudinal acoustic modes, w is the speed of sound in the gas at a specific temperature and pressure. Coupling equation (3) into equation (4), the speed of sound is then calculated. The values of $w(p)$ measured on an isotherm are fitted by the acoustic virial equation to determine w_0 the speed of sound in the ideal gas at the isotherm's temperature.

In this work, we measured four TM microwave modes and five purely longitudinal acoustic modes. For simplicity in the following text, we adopt the non-standard notation: Ms ($s = 1$, 2, 3, 4) for the microwave modes $(s\,0\,1)_{TM}$ and Al ($l = 1$, 2, 3, 4, 5) for the acoustic modes $(l00)$.

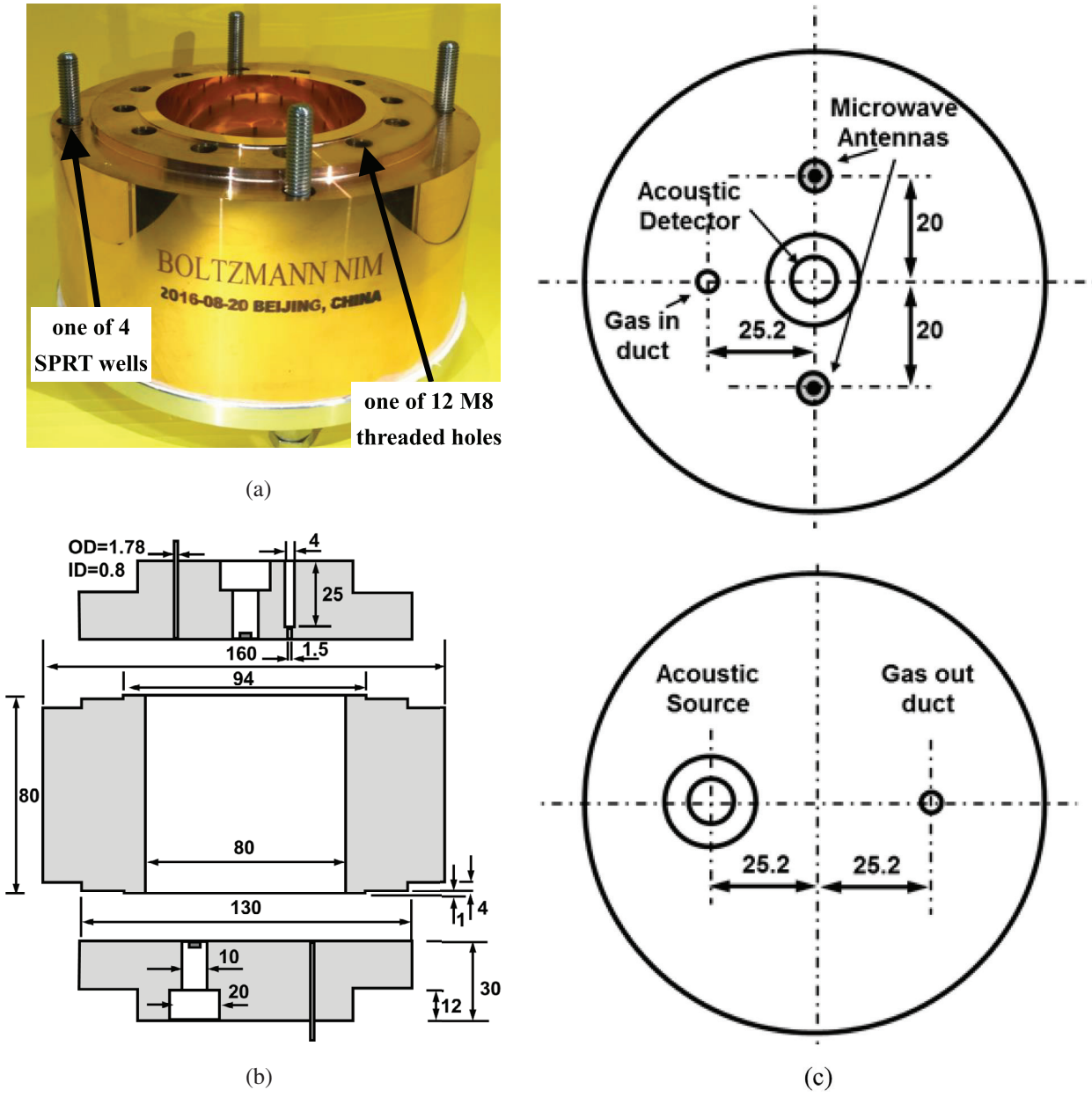

Figure 1. (a). Cylinder cavity made of oxygen-free copper. (b) Cross section of the cavity. Dimensions are in millimeters. (c) The upper and lower endplates, as viewed from inside the cavity. All dimensions are in millimeters.

3. Experimental setup

3.1. Cylindrical cavity

For this work, we used a cylindrical cavity surrounded by an oxygen-free high-conductivity (OFHC) copper shell. The cavity had a nominal length of 80 mm, an inner diameter of 80 mm and an outer diameter of 160 mm. The pair of endplates was machined from the same billet OFHC copper that was used to make the cylindrical shell. Figure 1(a) is a photograph of the cylindrical shell and figures 1(b) and (c) are sketches of the cross section of the cavity and the endplates. The 1 mm step at each end of the cylinder nearly sealed the endplates to the cylinder. This minimized the possible flow of impurities from the bolts' holes into the cylinder and the leakage of the acoustic and the microwave fields through the mating surfaces and out of the cavity.

The cavities and endplates were fabricated with a high-precision diamond-turning machine. The manufacturer specified that the cross-section of the cylindrical shell was round and coaxial within 0.4 μm. The cylindrical shell and the endplates were machined to a roughness of 0.01 μm. The flatness of inner surfaces of the endplates were machined within 0.2 μm. The surfaces of the endplates were parallel within 1 μm. Two thermometers were embedded in diagonally opposite wells in the cylindrical shell. (In figure 1(a), the wells are occupied by the steel screws.) One thermometer was inserted in the upper end and the other was inserted in the lower end.

As shown in figures 1(b) and (c), the upper endplate accommodates the gas inlet duct, the microwave antennas, and the acoustic source transducer. The lower endplate accommodates the gas discharging duct and the detecting acoustic transducer. In this work, we used the same type of piezoelectric

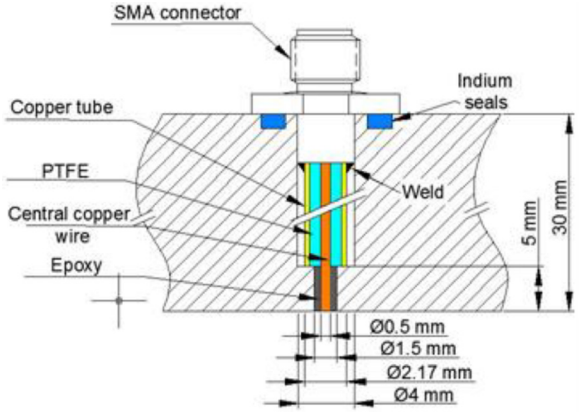

Figure 2. Sketch of the microwave antenna inserted into a port in the upper endplate.

transducers (PZTs) and the same transducer electronics that we used previously [11, 13]. The dimensions of the PZTs and the blind wells accommodating them were also the same as those reported previously.

Straight wire antennas (0.5 mm diameter) were used to drive and detect the TM modes. Figure 2 is a schematic cross-section of an antenna in its port in an endplate. The antenna itself was the end of the central copper conductor of a commercial coaxial cable from which the insulation and shield layers had been cut off. We inserted the cable into the port from the outside and forced the remaining PTFE insulation on the cable against the step. The space between the naked conductor and the port was filled with epoxy that insulated and immobilized the antenna and prevented gas from flowing through the port. The epoxy and antenna were machined to be flush with the inner surface of the endplate. The outer end of the cable was welded to an SMA connector. This design of the antennas is an improvement over our earlier designs [15] because it allows diamond turning of the entire inner surface of each endplate.

The ducts that continuously brought argon into and out of the cavity were designed to minimize their perturbations to the acoustic and microwave frequencies. As indicated by the dashed curves in figure 3, a section of each duct was an OFHC copper tube (0.8 mm I. D., 1.78 mm O. D., 1 m long) that was shrink-fitted into an endplate. The argon-inlet duct was fitted into the upper endplate at the location (0.628 a, 0°) and the argon-outlet duct was fitted into the lower endplate at the location (0.628 a, 180 °). The shrink-fitted ends of both copper tubes were machined flush with the inner surfaces the endplates.

Figure 3 is a sketch of the gas-handling system. The argon-inlet copper tube led from the cavity through a seal in the pressure vessel surrounding the resonator and then joined a stainless-steel tube (6.35 mm O. D., 2 m long) that, in turn, led to a mass flow controller (MFC) and then to the gas-supply manifold. The argon-outflow duct was coiled within the pressure vessel and discharged the argon into the pressure vessel. A larger outlet tube connected the pressure vessel to a MFC (functioning as a back-pressure regulator) and a vacuum pump. The upstream MFC and the back-pressure regulator allowed us to take measurements while clean argon flowed continuously from the argon supply manifold to the vacuum pump.

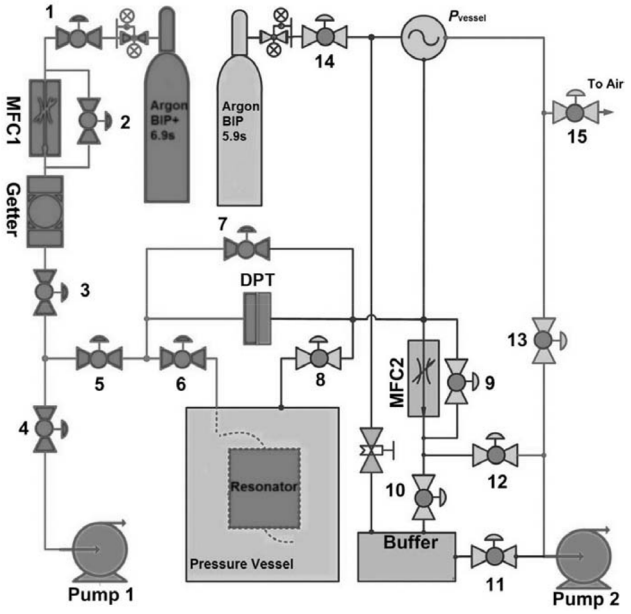

Figure 3. Sketch of the gas handling system. DPT denotes the differential pressure gauge and MFC denotes the MFC. The dotted curves inside the pressure vessel represent the inlet and outlet capillary ducts.

This continuous-flow arrangement contrasts with our previous work. Previously, we filled the cavity (and the pressure vessel) to a maximum pressure on each isotherm. We measured the speed of sound $w(p)$ of the gas in the cavity and then pumped some argon out of the cavity to reduce the pressure. This was done in steps. On each step, $w(p)$ was measured in the fraction of the initial argon that remained in the cavity.

As we did previously, the endplates were clamped to the shell of the cylindrical cavity by 12 M8 bolts, each made of oxygen-free copper with an 8 mm nominal diameter. The torque applied to the bolts was 4 N · m. Because the copper bolts were very soft and subject to cold welding, the resonator was initially assembled with stainless-steel bolts torqued to 4 N·m. Then, the stainless-steel bolts were replaced by copper bolts, one by one. Thus, the assembled resonator was made entirely of copper and all of its parts were expected to have identical thermal expansions between room temperature and T_{TPW} the temperature of the triple point of water. Thus, we did not expect the cavity's shape to change when it was cooled from ambient temperature to T_{TPW}.

3.2. Temperature measurement system

We read and monitored the temperature of the cavity using two thermometer assemblies embedded into diagonally opposite sides of the cylindrical shell. The thermometers were 25 Ω standard capsule-type platinum resistance thermometers (Hart[5] 5686-001-B model, HS 196 and HS 159).

[5] In order to describe materials and procedures adequately, it is occasionally necessary to identify commercial products by manufacturers' name or label. In no instance does such identification imply endorsement by China's National Institute of Metrology or the USA's National Institute of Standards and Technology, nor does it imply that the particular product or equipment is necessarily the best available for the purpose.

Each thermometer had the outer diameter of 5.5 mm and the length of 35 mm. As in our previous work [11], we enclosed each thermometer with a copper sleeve. The sleeve allowed us to move the thermometer assemblies between a triple-point-of-water (TPW) cell and the wells in the resonator's wall without disturbing the thermometers or changing their thermal resistance. The sleeve was also a shield against electrical noise. Each sleeve (100 mm long, 10 mm O. D., 5.6 mm I. D.) had a sensing head 40 mm long and was sealed at one end. Each thermometer was covered with thermally conducting grease and inserted into the open end of a sleeve. Then, a cap was screwed onto the sleeve to hold the thermometer against the inner wall and blind end of the sleeve. The four leads of each thermometer passed through a thin stainless-steel tube (2.13 mm I. D., 500 mm long) to a sealed feed-through. After connecting the leads, assembling the sleeve, tube, and feed-through, the thermometer assembly was evacuated and purged with pure argon gas in five times. Finally, the assembly was filled with pure argon gas to 110 kPa and sealed with a valve.

In our previous work [11], the temperature difference between the two thermometers was 0.047 mK when they were inserted in wells in a similar cylindrical shell made of bearing steel and near T_{TPW}. In this work, the temperature difference across the copper shell was 0.04 mK, which is equivalent to $0.15 \times 10^{-6}\ T_{\mathrm{TPW}}$. Thus, the temperature difference contributed the fractional uncertainty 0.15×10^{-6} to $u_{\mathrm{r}}(k_{\mathrm{B}})$.

3.3. Gas handling and pressure measurement system

Most of the gas supply manifold is unchanged since our previous report [11]. The gas manifold has been filled with clean argon since we began experiments in 2009. Before each experiment, the manifold was tested for leaks at 1 MPa. The manifold contained a getter (SAES model GC50) to remove reactive impurities from the argon gas. Prior to the present experiments, we replaced the getter with a new one.

As mentioned above, we installed two MFCs, one upstream and one downstream of the cavity, to control the gas flow rate through the cavity. A differential pressure gauge (MKS Baratron model 616A, 100 torr (13.3 kPa) full scale), labeled DPT in figure 3, measured the difference between the pressure upstream of the cavity's inlet duct and the pressure in the pressure vessel. The DPT readings were fed back to the MFCs through a digital PID controller programmed in LabVIEW. The flow rate was controlled to generate an 80 Pa pressure drop across the DPT. The volume flow rate varied from 3 SCCM at 50 kPa to 20 SCCM at 550 kPa. (We define 1 SCCM = $\mathrm{cm}^3\ \mathrm{min}^{-1}$ at the pressure 101.325 kPa at 0 °C.) Because the inlet and outlet ducts to the cavity are nearly identical (so the flow impedances are nearly identical), we assumed that, the pressure inside the cavity was 40 Pa higher than the pressure in the pressure vessel surrounding the cavity. An absolute pressure gauge (Ruska model 7250 xi, 0 kPa to 600 kPa) controlled the pressure inside the pressure vessel. We did not detect changes in the acoustic resonance frequencies when the gas flow was stopped. Inside the cavity, the pressure variations were within ±2 Pa.

4. Measurements

4.1. Measuring the length of the cavity

In this work, we measured the length of the cylindrical cavity using the procedures that we described in [15]; however, we made one change (in contrast with [15]) because we are now concerned with both acoustic and microwave frequencies. Therefore, as discussed in section 3.1 and shown in figure 2, we filled the slit between the central conductor and the endplate with epoxy. The epoxy eliminated acoustic perturbations from the slit and prevented the central conductor from moving. We excited the microwave modes with a network analyzer (Agilent E8362C) frequency-referenced to the 10 MHz standard frequency provided by a GPS clock. The output of the analyzer was transmitted to the antennas through a 3 m long flexible microwave cable and an SMA feedthrough mounted at the top endplate of the pressure vessel.

The four non-degenerate TM modes, Ms (s = 1, 2, 3, 4) were used to measure the cavity's length in the vacuum and at various pressures. For each mode, the network analyzer measured the complex values of $S_{21}(f)$ in the frequency band spanning $f_s \pm 5g_s$, where f_s is the frequency of the mode and g_s is the half-width of the mode. The resonant frequency and half-width were obtained by fitting the real and the imaginary parts of $S_{21}(f)$ with the function:

$$\boldsymbol{S}_{21}(\boldsymbol{f}) = \boldsymbol{u} + \boldsymbol{iv} = \frac{\mathrm{i}\boldsymbol{A}\boldsymbol{f}}{\boldsymbol{f}^2 - \boldsymbol{F}_s^2} + \boldsymbol{B} + \boldsymbol{C}\left(\boldsymbol{f} - \tilde{\boldsymbol{f}}\right) \tag{5}$$

where $\boldsymbol{F}_s = f_s + \mathrm{i}g_s$ is the complex resonant frequency of a mode under study, $\boldsymbol{A}$, $\boldsymbol{B}$ and $\boldsymbol{C}$ are complex constants obtained from the fitting, and f are the frequencies generated by the spectrum analyzer. For numerical purposes $\tilde{\boldsymbol{f}}$ is chosen to be an arbitrary constant close to the center frequency f_s.

The measured resonance frequencies differ from their ideal values because of imperfections of the cavity's shape, finite (not infinite) electrical conductivity of the walls surrounding the cavity, gas ducts, antennas, joints between the cylindrical shell and the endplates, etc. Many of these non-idealities dissipate the electromagnetic energy thereby increasing the half-widths of the resonances. We denote the complex resonance frequency $\boldsymbol{F}_s$,

$$\boldsymbol{F}_s = \boldsymbol{f}_s + \mathrm{i}\boldsymbol{g}_s = \boldsymbol{f}^0 + \sum_{j=1}^{n}\left(\Delta\boldsymbol{f}_j + \mathrm{i}\Delta\boldsymbol{g}_j\right) \tag{6}$$

where Δf_j and Δg_j account for the frequency perturbations contributed by the jth imperfection.

We measured the microwave resonance frequencies Ms (s = 1, 2, 3, 4) at T_{TPW} and at the nominal pressures: 50 kPa, 75 kPa, and (100 + 50 m) kPa where m = 0, …, 9. Figure 4 displays a typical 9 h-long record of 200 repeated measurements of the frequency M2 at 50 kPa during measurements of the acoustic frequencies A1, A2, A3, A4, and A5. The measurements of M2 are separated into four sets of 50 measurements. In each set, the M2 frequencies span the fractional range 0.02×10^{-6}, or less. The fractional difference between the average of the 1st set and the 4th set was 3.7×10^{-9}; this difference is equivalent to the thermal expansion of copper

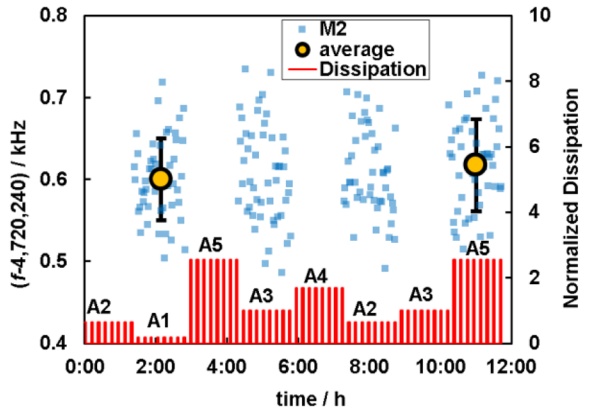

Figure 4. Blue points: time-dependence of microwave resonance frequency M2 at 50 kPa while acoustic frequencies A1 … A5 are measured. Yellow dots are mean values of M2, the error bars are the standard deviation. Vertical red bars: normalized dissipation in acoustic source-transducer.

caused by a 0.2 mK temperature change. Thus, figure 4 is evidence of the stability of the thermostat and of the cavity's length.

Figure 4 displays evidence that the power dissipated in the acoustic source transducer did not generate significant temperature changes, even in the worst case (lowest pressure). In figure 4, the red shading is the normalized power dissipated in the source transducer while the modes A1, … A5 were repeatedly measured during a 9 h-long interval. It took about 3 min to acquire the data for each acoustic resonance frequency. After each acoustic measurement, the power to the source transducer was turned off for 8 min; then, the next acoustic frequency measurement began. During the same 9 h-long interval, the frequency of the microwave mode M2 was also repeatedly measured. The average value of M2 changed (17 ± 53) Hz. (Here the uncertainty is the standard deviation σ.) The change in M2 corresponds to a fractional length change of 3.7×10^{-9} or a fractional temperature change 7×10^{-7}. In figure 4, M2 does not have a visible time dependence, even though the power dissipated in the acoustic source was changed by a factor of 5.

In [15], we estimated the perturbations Δf_j and Δg_j for a cylindrical cavity resulting from the finite electrical conductivity, gas ducts, slits between the endplates and the cylindrical cavity, and the microwave antennas. For the modes that we studied, the largest perturbations were generated by electrical conductivity. As described in [15], we corrected the complex measured frequencies M1, M2, M3 and M4 for the conductivity and the other principal perturbations.

After correcting the measured frequencies for the calculated perturbations and the calculated index of refraction of argon [24], we determined the cavity's length at each pressure at T_{TPW} by fitting M1, M2, M3, and M4 using the procedure described in [18, 19]. The results are shown in figure 5. The relative deviations of the measured frequencies from their mean values calculated from the fitting result of L and a are shown in figure 6. The relative standard error of the length from the linear least square fitting of equation (3) is 0.30×10^{-6}, which appears in the uncertainty budget for $u_{\mathrm{r}}(L)$ in table 1.

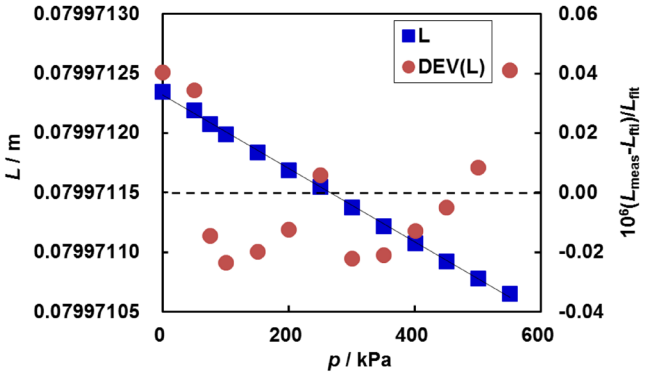

Figure 5. Linear fit to the cavity's length L as a function of pressure (left scale) and fractional deviations from fit (right scale).

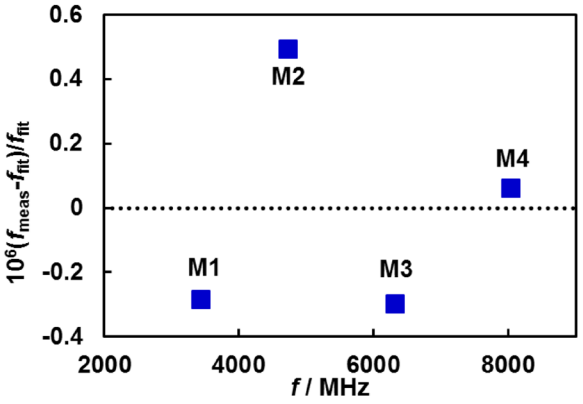

Figure 6. Relative deviations of measured microwave frequencies from fitting function.

Table 1. Relative uncertainty budget of measurements of the cavity length.

Uncertainty sources	$10^6 u_{\mathrm{r}}(L)$
Fitting of the frequencies	0.04
Estimate of surface electric resistivity	0.38
Perturbations of ducts and probes	0.07
Perturbations of non-conducting layer	0.10
Mode dependence	0.30
Total	0.50

The fractional deviations from the linear fit were less than $\pm 0.04 \times 10^{-6}$. These small deviations make a negligible contribution to the uncertainty budget of $u_{\mathrm{r}}(k_{\mathrm{B}})$.

The excess half-width $\Delta g = (g_{\mathrm{meas}} - g_{\mathrm{cal}})$ denotes the difference between the half-width of a measured microwave resonance and its value, calculated from the resistivity of copper at the TPW, $\rho_{\mathrm{e}} = 1.543 \times 10^{-8}\ \Omega$ m [25] which has a relative uncertainty of 5%. As shown in figure 7, the values of Δg decrease with increasing frequencies. Thus, the measured resonance of M1 had the largest excess half-width. Figure 7 displays the excess half-widths of the four modes at 550 kPa. The relative differences among values of Δg from 50 kPa to 550 kPa were within $\pm 5 \times 10^{-8}$.

Our model for the perturbation $\Delta g/f$ due to microwave waveguides, gas filling holes, acoustic transducers and the taper of the cylinder showed a result less than 0.5×10^{-6}, which could not explain the excess half-widths we observed.

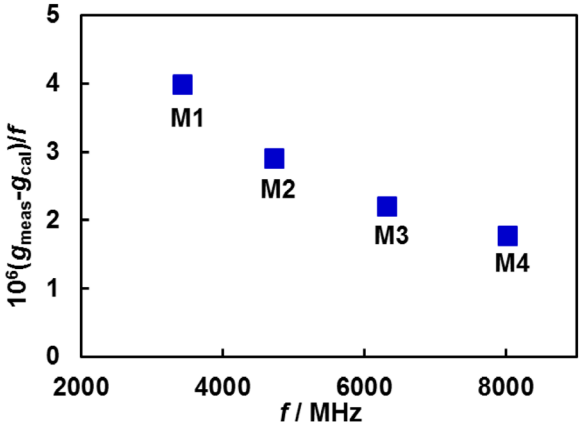

Figure 7. The excess half-widths of four microwave resonances.

Table 2. (a) Pre-calibration of thermometer. (b) Post-calibration of thermometer.

	HS 196
(a)	
Resistance (Ω) at 0 mA	25.443 761 21
	25.443 767 21
	25.443 771 10
	25.443 764 12
Average (Ω)	25.443 765 91
Standard deviation (Ω)	4.24×10^{-6}
(b)	
Resistance (Ω) at 0 mA	25.443 757 00
	25.443 758 73
	25.443 762 95
Average (Ω)	25.443 759 56
Standard deviation (Ω)	3.06×10^{-6}

However, we note that the spread among the values of Δg in figure 7 is much larger than the spread among the frequency deviations in figure 6. Thus, it is unlikely that the phenomena that determine Δg have a significant effect on the frequencies and so the uncertainty budget (table 1) does not include a contribution from Δg.

4.2. Temperature measurement

We followed the same procedure described in [11] to calibrate the two thermometers at T_{TPW}. An ASL F900 bridge was used to measure the ratios of the thermometers' resistances to the resistance of a 100 Ω standard resistor (Tinsley 5685A). The two thermometers were calibrated before and after being installed in the resonators. We named the two processes as the pre- and the post- calibrations. Table 2 lists the calibration data.

The calibrations were repeatable to less than 0.040 mK. The average pre- and post- calibrations differed by less than 0.025 mK. The repeatability, summed in quadrature with the difference between the pre- and post- calibrations contributed a type B relative uncertainty of 0.17×10^{-6} to $u_{\mathrm{r}}(k_{\mathrm{B}})$ in table 5.

As in our previous work [11], the Type B uncertainty of our realization of T_{TPW} in our triple-point cell was estimated

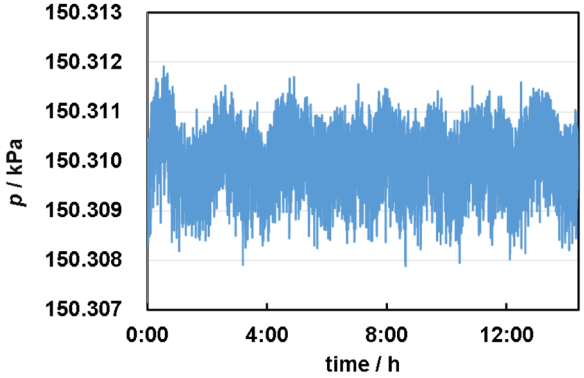

Figure 8. Typical pressure fluctuations in the cavity during the acoustic measurments.

to be 0.050 mK. This uncertainty contributed a relative uncertainty of 0.18×10^{-6} to $u_{\mathrm{r}}(k_{\mathrm{B}})$. For this triple-point cell, the calculated hydrostatic pressure effect was 0.182 mK; the thermometer calibration was corrected for this. We measured the axial temperature gradient of the thermometer assembly by pulling up each thermometer along the well of the TPW cell. The axial gradients were -1.120 mK m^{-1} or less. The gradient contributed a bias for the calibration value of 0.056 mK by taking into account the 100 mm long sleeve, which contributes a fractional uncertainty of 0.21×10^{-6} to $u_{\mathrm{r}}(k_{\mathrm{B}})$.

The total uncertainty from temperature measurement contributes a fractional uncertainty of 0.36×10^{-6} to $u_{\mathrm{r}}(k_{\mathrm{B}})$ including 0.17×10^{-6} from the repeatability of the calibration, 0.21×10^{-6} from the gradient of the TPW cell, 0.15×10^{-6} from the temperature gradient of the resonator and 0.18×10^{-6} TPW realized by the reference cell.

4.3. Pressure measurement

As described in section 3.1, we used a LabView program to control the pressure in the pressure vessel. The pressure fluctuations inside the cavity were within ±2 Pa, as shown in figure 8.

Our differential and absolute pressure gauges were calibrated against NIM's pressure standards. The long-term drift of the absolute pressure gauge was less than 30 Pa over the duration of the experiment. The drift of the differential pressure gauge was within 10 Pa. In a worst case, a 40 Pa drift causes a fractional change of 1×10^{-7} in w_0^2. This change accounted for a fractional contribution of 1×10^{-7} to $u_{\mathrm{r}}(k_{\mathrm{B}})$.

4.4. Sample gas and molar mass

For the measurements reported in this paper, we used the 'BIP Plus' grade argon supplied by Air Products Inc. The 'BIP Plus' argon was taken from the same container used for the measurements reported by us in [11]. The average molar mass of this 'BIP Plus' argon was determined by mass spectrometry traceable to the 2010 analysis of an argon reference carried out by the Korea Institute of Standards and Science (KRISS) [13]. Later, in 2014, KRISS conducted the historically important analyses [26] of 15 argon samples including several 'BIP

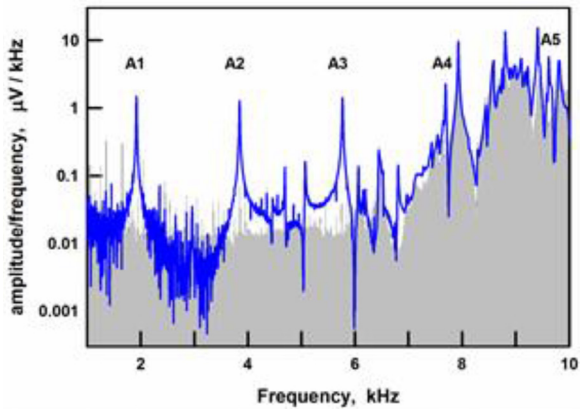

Figure 9. Spectrum of the evacuated resonator (solid gray) and spectrum of the resonator filled with argon at 75 kPa and TPW temperature (blue line).

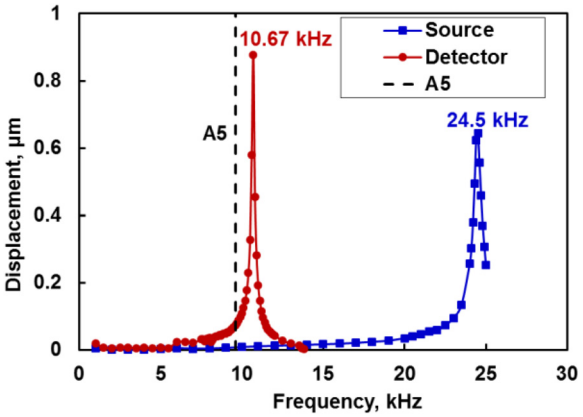

Figure 10. Spectra of the acoustic transducers.

Plus' samples provided by the authors and the research group of the National Physics Laboratory (NPL). The 2014 analysis [26] led to two corrections to the 2010 results [13]. One correction originated in the misquoted value of $^{40}Ar/^{36}Ar$ and the other correction originated in the mass discrimination correction K for the mass spectrometer. Together, these two corrections reduced the molar mass by the fraction 0.39×10^{-6}. The corrected molar mass of argon from NIM's 'BIP Plus' cylinder is 39.947 794 g mol^{-1}. The fractional uncertainty remains 0.77×10^{-6}.

We used an SAES Model GC50 getter to purify the argon. This getter reduces the mole fractions of reactive impurities (H_2O, CO, CO_2, O_2, H_2, N_2, CH_4 and other hydrocarbons) in argon to less than 0.01 parts per million. The concentrations of the noble gas impurities in the BIP grade and the BIP Plus grade argon had been studied in [8]. This study set upper bounds to the mole fractions of these gases in argon: 0.01×10^{-6} for Kr and Xe, 0.03×10^{-6} for Ne, and 0.01×10^{-6} for He. These bounds lead to the uncertainties $u_r(w_0^2)$ and $u_r(k_B) = 0.03 \times 10^{-6}$.

4.5. Acoustic measurements

4.5.1. Spectrum of the evacuated resonator. The PZT acoustic source was scanned from 1 kHz to 10 kHz to record the spectrum of the mechanical vibrations of the evacuated resonator. Figure 9 compares the spectrum of the evacuated resonator with the acoustic spectrum of the cavity while it contained argon at 75 kPa and T_{TPW}. The vacuum spectrum shows numerous small peaks at the odd harmonics of the power-line frequency (50 Hz). Above 6.6 kHz, the vacuum spectrum shows several broad peaks which overlap the A4 and A5 acoustic resonances at 75 kPa. The mechanical vibrations of the resonator that generated these peaks in the vacuum spectrum might have coupled to the A4 and A5 acoustic resonances. The acoustic frequencies for the A4 mode have an anomalous pressure-dependence (i.e. a pressure dependence that differs from $w(p)$), which suggests that strong coupling did occur for this mode.

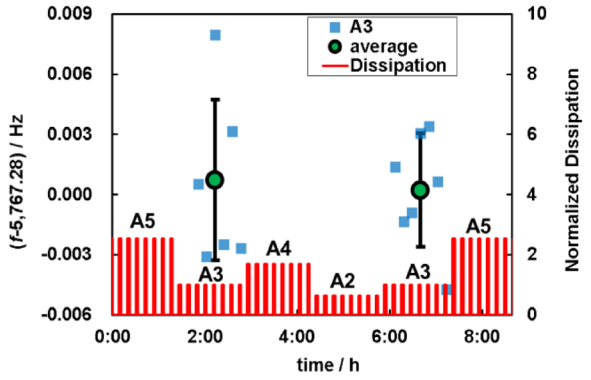

Figure 11. Blue squares: time-dependence of acoustic resonance frequency A3 at 50 kPa. Green circles are the mean values of A3. Vertical red bars: normalized dissipation in acoustic source-transducer.

4.5.2. Spectra of the acoustic transducers. The natural vibrations of the two piezo-electrical acoustic transducers were studied after installing the transducers in their blind ports in the endplates, but before bolting the endplates to the cylindrical shell. A function generator drove each transducer with a frequency sweep while laser interferometry measured the amplitude of the diaphragm's vibrations. Figure 10 displays the spectra for the source and the detector transducers. The detector transducer has a resonance near that of A5 mode. If the diaphragm resonance coupled strongly to the acoustic resonance, we would expect the A5 mode to have an anomalous pressure dependence. This was not seen. The resonance frequency of the source transducer is well separated from the acoustic modes studied in this work.

4.5.3. Effect of self-heating of PZT. The source PZT was driven with a sinusoidal waveform from an Agilent 33220A function generator with peak-to-peak voltages from 5 V at the highest pressure to 35 V for the A2 mode and 30 V for the other three modes at the lowest pressure. The calculated largest dissipation from the driven transducer is approximately 0.1 mW. We examined the effect of heat release by the PZTs at 50 kPa, the worst case of the effect. The microwave resonance frequencies were remarkably stable, varying by less than 3.7×10^{-9} over 9 h (figure 4). This small fractional difference means that we observed no effect of thermal expansion due to self-heating of the PZT.

Figure 11 shows the frequency of acoustic resonances of mode A3 measured twice in 5 h at 50 kPa, the pressure where the signal-to-noise ratio was worst. The relative standard deviations of the two sets of measurements were 0.69×10^{-6} and 0.49×10^{-6}. The fractional difference between the averages of two sets was 8.9×10^{-8}.

In summary, neither the microwave nor the acoustic measurements show any effect of heat released from the transducers.

4.5.4. Measurement of acoustic resonances. We used the method described in [11, 13] to determine the acoustic resonance frequencies f_N and the half-widths g_N. We stepped the source transducer through 13 synthesized, discrete frequencies in the increment of $g_N/4$ starting at $f_N - 1.5g_N$ and ending at $f_N + 1.5g_N$. Then we changed the step size to $-g_N/4$ and stepped back to $f_N - 1.5g_N$. For each mode, the frequency was swept upward and downward through eight cycles. Then we waited 1200 s for dissipating the heat generated by the source PZT before beginning a new sweep for another mode. At each mode, the complex voltage $V \equiv u + \mathrm{i}v$ generated by the detector transducer was measured by a lock-in amplifier (Stanford Research Systems model SR830). The 26 frequencies and complex voltages were fitted by the resonance function

$$V = \frac{\mathrm{i}fA}{f^2 - (f_N + \mathrm{ig_N})^2} + B + C\left(f - \tilde{f}\right) + D\left(f - \tilde{f}\right)^2 \tag{7}$$

where A, B, C and D are complex constants; $F_N = f_N + \mathrm{i}g_N$ is the complex resonance frequency of mode N under study. The real constant $\tilde{f}$ has no physical significance; it is set to a value near f_N to ensure that the fitting algorithm is numerically stable.

In [11, 13], we calculated the perturbations to the ideal frequencies of the pure longitudinal acoustic resonances in a cylindrical, gas-filled cavity. The perturbations considered were caused by the following effects: the viscosity, thermal conductivity, and mean-free-path of the sample gas, elastic motion of the cavity's walls, motion of the transducers, and motion of the gas in the ducts. These effects change the resonance frequencies and contribute to the half-widths of the resonances. The calculated perturbations were assumed to be independent of each other; therefore, their combined effect is the sum of the individual perturbations. (The calculated perturbations were first-order approximations except for the second-order approximation used to account for the viscous and thermal boundary layers where the gas meets the walls of the cavity.) We followed the procedures given in [11, 13] to calculate the perturbation corrections to the measured frequencies for every mode at every pressure.

The resonant frequencies corrected for the perturbations are labelled $f_{\mathrm{corrected}}$, such that $f_{\mathrm{corrected}} = f_{\mathrm{meas}} + \Sigma\Delta f_i$, where the subscript i denotes the various perturbations attributed to the above-mentioned effects.

The measurements of acoustic resonances were implemented at the temperatures near TPW and the target pressures. The measurements were adjusted to T_{TPW} and the target pressures by the linear relation:

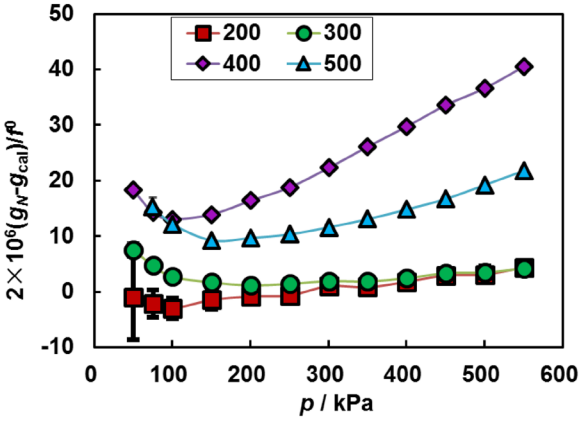

Figure 12. Excess half-widths of the acoustic resonances.

$$\frac{f_{\mathrm{corrected}}\left(T_{\mathrm{TPW}}, \langle p\rangle\right)}{f_{\mathrm{corrected}}\left(T_i, p_i\right)} = 1 + \left(\frac{1}{c^2}\frac{\mathrm{dc}^2}{\mathrm{dp}}\right)_{\mathrm{p}}\left(\langle p\rangle - p_i\right) + \left(\frac{1}{c^2}\frac{\mathrm{dc}^2}{\mathrm{dT}}\right)_{\mathrm{T}}\left(T_{\mathrm{TPW}} - T_i\right) \tag{8}$$

where the corrections for the temperature and pressure were on the order of 0.1 mK and 10 Pa, respectively.

We averaged the adjusted frequencies of the same mode to obtain a single frequency $f_{\mathrm{exp},l}(p)$ and the standard deviation which were used in the subsequent analysis.

4.5.5. Excess half-widths. In [11], we summarized the effects contributing to the half-widths of longitudinal acoustic modes of a gas-filled cylindrical cavity. In this work, we calculated the contributions to the half-widths from the thermal and viscous boundary layers and from the gas inlet and outlet ducts exactly as described in [11]. The sum of these calculated contributions is g_{cal}. The difference between the measured half-width of the mode N is denoted $\Delta g_N \equiv (g_N - g_{\mathrm{cal}})$ and called the excess half-width. Figure 12 displays the excess half-widths of the modes A2, A3, A4, and A5 as a function of the pressure. For modes A2 and A3, $\Delta g_N/f^0$ are less than 2.2×10^{-6} for the pressures ranging from 100 kPa to 550 kPa. For these modes, $\Delta g_N/f^0$ increases below 100 kPa, reaching 3.7×10^{-6} at 50 kPa for A3 mode. In [11], the values of $\Delta g_N/f^0$ for the modes A2 and A3 followed a similar trend above 200 kPa; however, the upturn at low pressures began at 200 kPa and was larger.

In figure 12, $\Delta g_N/f^0$ for modes A4 and A5 are larger than for A2 and A3 at all pressures. We speculate that these modes couple to the elastic modes of the empty copper shell. The spectrum of the evacuated resonator in figure 9 is evidence that shell modes occur at the frequencies of A4 and A5. Models for such coupling predict frequency perturbations that are linear functions of the gas pressure; it is plausible that the same phenomenon generates values of $\Delta g_N/f^0$ that are also linear functions of the pressure.

The A1 data had large, negative, excess half-widths $\Delta g/f^0$ at low pressures. Negative values of $\Delta g/f^0$ are inconsistent with known acoustic losses. Negative values of $\Delta g/f^0$ can occur if the resonance profile (complex voltage-versus-frequency data) is inconsistent with the profile of a single

Table 3. Fitted parameters and derived quantities.

Parameter	l	Unit	Value
A_0	2	$m^2 \cdot s^{-2}$	94 756.38(30)
	3	$m^2 \cdot s^{-2}$	94 755.90(24)
	4	$m^2 \cdot s^{-2}$	94 756.21(24)
	5	$m^2 \cdot s^{-2}$	94 755.76(22)
$10^4\, A_1$	2	$m^2 \cdot s^{-2} \cdot Pa^{-1}$	2.205(11)
	3	$m^2 \cdot s^{-2} \cdot Pa^{-1}$	2.251(10)
	4	$m^2 \cdot s^{-2} \cdot Pa^{-1}$	1.235(10)
	5	$m^2 \cdot s^{-2} \cdot Pa^{-1}$	2.346(10)
$10^{11}\, A_2$		$m^2 \cdot s^{-2} \cdot Pa^{-2}$	5.06(12)
$10^{-4}\, A_{-1}$		$m^2 \cdot s^{-2} \cdot Pa$	−5.0(1.3)
χ^2/ν			2.2
$10^4\, \langle A_1 \rangle$		$m^2 \cdot s^{-2} \cdot Pa^{-1}$	2.009
$\langle A_0 \rangle$		$m^2 \cdot s^{-2}$	94 756.06(38)
R		$J \cdot mol^{-1} \cdot K^{-1}$	8.314 458(35)
$10^{23}\, k_B$		$J \cdot K^{-1}$	1.380 6483(58)

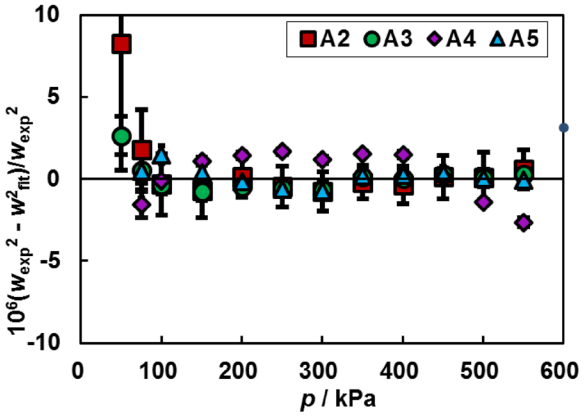

Figure 13. The relative deviations of the squared speed of sound from weighted fitting of the values of $(w_{\mathrm{exp},l})^2 - A_3p^3$ to the 10-parameter surface $A_{0,l} + A_{1,l}p + A_2p^2 + A_{-1}p^{-1}$, where the subscript '$l$' identifies the mode-dependent parameter.

acoustic resonance. The negative values of $\Delta g/f^0$ from the A1 mode remained even when we accounted for the expected frequency-dependence of g. Thus, they indicate that some phenomenon is omitted from the model for the experiment, even in the limit of zero pressure. As an example of such a phenomenon, we note that the model for these measurements does not include the coupling of the PZT transducers to each other even when the shell is evacuated. As shown by the shaded area in figure 9, this coupling was easily observed. Thus, we didn't use A1 for the present determination of k_B.

4.5.6. Fitting f(T, p, mode) surface. The experimental speeds of sound $w_{\mathrm{exp},l}$ were obtained by correcting the values of $f_{\mathrm{exp},l}$ for the known perturbations to obtain $f_{\mathrm{exp},l,\mathrm{corr}}$ and then inserting $f_{\mathrm{exp},l,\mathrm{corr}}$ in equation (4). Then, we fitted the values of $(w_{\mathrm{exp},l})^2 - A_3p^3$ by the polynomial function of pressure:

$$(w_{\mathrm{exp},l})^2 - A_3p^3 = A_{0,l} + A_{1,l}p + A_2p^2 + A_{-1}p^{-1}. \quad (9)$$

In equation (9) the Boltzmann constant is related to A_0, the average of $A_{0,l}$ through $A_0 \equiv u_0^2 = N_A\gamma_0 k_B T_{TPW}/M_{Ar}$. When fitting equation (9), A_2 and A_{-1} were mode-independent

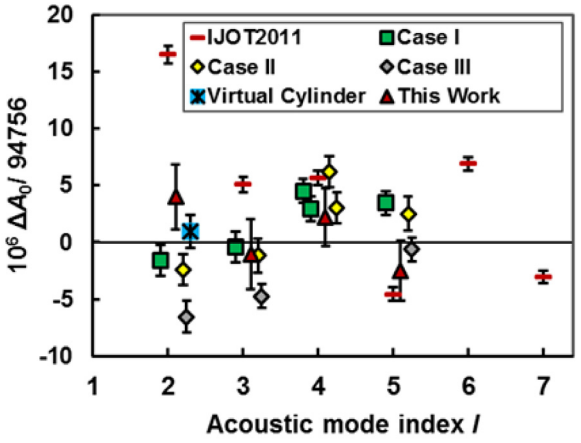

Figure 14. Values of relative $\Delta A_0 = A_0 - 94\,756$ from six different data sets. For clarity, most plotted points are horizontally displaced from integer values of l.

adjustable parameters. (A_2 is closely related to the third acoustic virial coefficient and A_{-1} accounts for imperfect energy and momentum accommodation between the argon and the copper walls of the cavity [27].) A_3 was fixed at the value 1.45×10^{-18} m^2 s^{-2} Pa^{-3} taken from [7], and $A_{1,l}$ took the values $A_{1,2}$, $A_{1,3}$, $A_{1,4}$, and $A_{1,5}$ for modes A2, A3, A4 and A5, respectively. When fitting equation (9), we weighted each value of $(f_{\mathrm{exp},l,\mathrm{corr}}L/l)^2$ by the same method as [11]. Table 3 lists the results from the fitting.

The values of $A_{0,l}$ for $l = 2,4$ are larger than the values of $A_{0,l}$ for $l = 3,5$. We cannot explain this even-odd mode dependence. (If the center-of-mass correction is in error, the values of $A_{1,l}$ will have an even-odd dependence [11].)

The mode A4 mode was strongly coupled to a shell mode as evidenced by the large values of its excess half-width $\Delta g_N/f^0$. in figure 12 and by its anomalous value of $A_{1,4}$ in table 3. In the simplest models, the frequency perturbations from the elastic modes of a shell are linear functions of the pressures [24]. However, figure 13 shows the deviations of $w_{4,\mathrm{exp}}^2$ from the fit by equation (9) have a definite negative curvature at pressures above 400 kPa, where both the coupling is strongest and the signal-to-noise ratio is best. Because of the good signal-to-noise ratio, this curvature was given a similar weight during fitting and it explains why the value of the reduced chi-squared χ^2/ν in this work is larger than that in our previous publications [11]. The negative curvature requires a better theory for the coupling of a gas mode to an elastic shell mode.

The uncertainty budget for the determination of k_B is listed in table 5. The k_B determined from the copper resonator was estimated to be $1.380\,6483(58) \times 10^{-23}$ J K^{-1} with the relative standard uncertainty of 4.2×10^{-6}.

5. Weighted mean of the different k_B determinations

The authors have previously published four, nearly-independent, determinations of k_B, in addition to the present determination of k_B [11, 13, 14]. Here, we provide an intuitive discussion of the correlations among the uncertainties of

Table 4. Primary differences between five data groups.

Label (ref)	IJOT2011 [13]	Case I [11]	Case II, III [11]	Virtual Cylinder [14]	This work
Cavity length/mm	130	80	80	80/160	80
Side wall	Steel	Steel	Steel	Steel	Copper
Endplates	Fused silica	Fused silica[a]	Fused silica[a]	Fused silica	Copper
Argon	BIP	BIP-Plus	BIP, BIP-plus	BIP-plus	BIP-plus

[a] Endplates were exchanged between Case I and Case II.

these earlier measurements and we also determine a weighted mean value of k_B that includes the earlier measurements and the present results.

By far, the largest uncertainty in our earlier determinations as well as our present work results from the inconsistent values of A_0 deduced from the various acoustic modes. Figure 14 displays the values of A_0 that we will average. As discussed in section 4.5.5, figure 14 does not include the values of A_0 deduced from the A1 mode because these values had large negative excess half-widths.

We cannot explain the inconsistencies among the values of A_0; however, they are reproducible for each resonator. Therefore, we treat the values of A_0 as if they were distributed randomly among the modes.

In figure 14, the data are plotted in 6 groups. Table 4 lists the primary differences between the groups. The groups labelled Cases I, II, and III were all obtained using an 80 mm-long cavity with steel sides and fused silica endplates. Between Case I and Case II, the resonator was disassembled and the endplates were interchanged. This required cycling the apparatus from T_{TPW} to ambient temperature and a new length measurement. Between Cases II and III, the argon supply was changed [11]. Thus, it is not surprising that the values of A_0 in figure 14 for Cases II and III are correlated, we consider the Case II and Case III as one measurement because the uncertainty from the gas is not the major uncertainty contribution here.

Despite significant changes in resonator design and the way in which the cylinder length is determined, the average of A_0 is substantially unchanged as shown in figure 14. This is the justification for calculation of the weight mean of our five k_B determinations. Therefore, we analyzed the correlations of the uncertainty entries of the variant determinations. According to the correlation analysis, we combined the result given in section 4 with our four previous results to calculate a global weighted mean of our k_B determinations.

In figure 14, the uncertainty bars for A_0 account for the random error in A_0 given in table 5. The data set of IJOT2011 do not overlap each other. To compute the weighted average, these values of A_0 were averaged and their standard deviation from the mean A_0 appears in table 5 as inconsistency among modes for the IJOT2011 set. The values of A_0 for Cases I, Case II and III, and this work were treated in the same way.

The measurement from the virtual cylinder in 2015 [14] used a combination of the A2 mode of 80 mm resonator and the A4 mode of 160 mm resonator, which occur at the same frequency, to decrease the perturbations from the cavities' ends. In principle, the A3 and A4 modes of the 80 mm resonator could be paired with the A6 and A8 modes, respectively, of the 160 mm resonator to achieve the same reduction of end effects. However, the A2–A4 mode combination was the only virtual resonator mode that we could use. Because the two resonator shells had different vibrational spectra due to the different lengths, the perturbations due to coupling between the gas modes and the shell modes were very different for the two resonators, the dissimilarity becoming more pronounced with increasing frequency. Additionally, the A3–A6 mode pair has mixed symmetry about the mid-plane of each resonator (the A3 mode has odd symmetry and the A6 mode has even symmetry), therefore the type of coupling between the acoustic modes and the shell modes in the two resonators was very different and dominated the perturbations on the acoustic frequencies. Such asymmetries between the two resonators complicated the virtual resonator concept in ways that we could not easily model. Fortunately, the frequency of the A2–A4 virtual resonator mode was far enough below the vibrational modes of both resonators that the virtual resonator model could be used. Because we have only one virtual resonator mode, we estimate the uncertainty contribution to k_B from A2–A4 virtual cylinder as the standard deviation between the values of A_0 from the A2 and A4 modes considered separately. The uncertainty from the boundary layer correction is smaller because the effects from the endplates are minimized by the virtual cylinder. The uncertainty budget is listed in table 5.

The least-squares method for the best estimation of constants of partially correlated measurement uncertainties is given in the paper 'CODATA Recommended Values of the Fundamental Physical Constants: 1998' [22, 23]. The core of the procedure is the formulation of the weight matrix through accounting for the correlations. We applied the method to derive the weighted mean of the five determinations of k_B by the c-AGT. For this purpose, we identified the correlations among the measurement uncertainties of the parameters in equation (1) by referring to reference [28]. For brevity, we labeled the first determination reported in reference [13] as k_B1, the determinations in Case I, reported in reference [11] as k_B2, Case II and III [11] as k_B3, virtual cylinder [14] as k_B4, and the current determination as k_B5. The procedures for measuring the cavity lengths for the five determinations fall into two groups. The first four determinations relied on two-color laser interferometry to measure the distance between the endplates. The endplates were made of optical-quality quartz and the cylindrical shells were made of bearing steel. These four determinations form the first group. The second group, consisting only of the determination k_B5, differs from the first group because the length of the cavity was determined from the frequencies of several microwave modes of the cylindrical cavity. For this cylindrical resonator, both the cylindrical shell and the pair of endplates were made of OFHC copper. Determinations k_B1 and k_B3 (Case III) were made from samples of the same 'BIP' grade argon whose molar mass was analyzed in KRISS in 2010 by mass spectrometry referenced to a gravimetrically prepared mixture [29]. Determinations k_B2, k_B3 (Case II), k_B4, and k_B5 used the 'BIP Plus' grade

Table 5. Different determinations of k_B with their uncertainty budget and correlations.

	k_B1	k_B2	k_B3	k_B4	k_B5
Uncertainty source			$10^6 \times u_r(k_B)$		
1. Temperature measurement					
Thermometer calibration	0.48	0.36^C	0.36^C	0.36^C	0.17
Thermometer gradient	0.21	0.21^C	0.21^C	0.21^C	0.21^C
Temperature inhomogeneity	0.73	0.18^C	0.18^C	0.18^C	0.15
TPW realization	0.18^C	0.18^C	0.18^C	0.18^C	0.18^C
2. Pressure measurement	0.10^C	0.10^C	0.10^C	0.10^C	0.10^C
3. Avogadro constant,	0.01^C	0.01^C	0.01 ^{C}	0.01^C	0.01^C
4. Molar mass					
Noble gas impurities[a]	0.03^C	0.03^C	0.03^C	0.03^C	0.03^C
Isotopic abundance ratios	0.70^C	0.70^C	0.70^C	0.70^C	0.70^C
Mass spectrometry	n/a	0.32^C	0.32^C	0.32^C	0.32^C
5. Length measurement					
5.1 Optical measurement					
Average cavity length	0.45	1.08	0.81	0.86	n/a
Optical-acoustic difference	0.31	0.50^C	0.50^C	0.50^C	n/a
Two—color interferometry	0.46^C	0.58^C	0.58^C	0.58^C	n/a
5.2 Microwave measurement	n/a	n/a	n/a	n/a	
Fitting of the frequencies					0.08
Surface electric resistivity					0.76
Ducts and probes					0.14
Non-conducting layer					0.20
Mode inconsistency					0.60
6. Corrected frequencies					
Boundary layer corrections	0.40	0.40	0.40	0.20	0.40
Random error in A_0	0.67	1.19	1.37	1.48	2.67
7. Inconsistency among modes	7.64	2.65	3.15	2.54	2.96
Combined uncertainty	7.86	3.35	3.82	3.36	4.22
$10^{23} \times k_B$ (J K^{-1})	1.380 650(11)	1.380 6498(46)	1.380 6460(53)	1.380 6486(46)	1.380 6483(58)

[a] We assumed that mole fractions of the noble gas impurities in BIP-grade and BIP-Plus-grade argon were: Kr and Xe, 0.01×10^{-6}; neon $< 0.03 \times 10^{-6}$; helium $< 0.01 \times 10^{-6}$. These impurity concentrations contribute to $u_r(w^2) = 0.03 \times 10^{-6}$. See section 4.4 and [8].

argon sampled from a single container. The molar mass of the 'BIP Plus' grade argon was analyzed by mass spectrometry with reference to the 'BIP' grade argon [11]. The relative standard uncertainty for the measurement of the molar mass of the sample in 'BIP' grade argon was 0.70×10^{-6} given by KRISS. The analysis with the gas chromatography-mass spectrometry system MAT 271 yielded an additional uncertainty of 0.32×10^{-6}. The values of k_B in table 5 were determined using the correct isotopic ratios and the Avogadro constant from [6].

According to equation (1), the uncertainty contributions to the determination of k_B are catalogued into seven sets as shown in table 5. By referring to reference [28], we outline in table 5 the correlation against the corresponding uncertainty contribution to $u(k_B)$. We summed up each set in the items accounting for the detailed uncertainty contributions. We marked the correlations in superscript '**C**'. The entries in a given row of table 5 marked with 'C' are completely correlated with each other, whereas the entries without a 'C' are not correlated at all with other entries in that row. The entries in different rows of table 5 are not correlated with each other.

In table 5, some rows had all five entries correlated because they shared the same values, the same analysis result or the measurements conducted with the identical facilities. The measurements for k_B2, k_B3 and k_B4 were conducted sequentially in which the same thermometers were shared. Accordingly, the uncertainty contributions due to thermometer calibration given in table 5 were completely correlated for those three measurements. The measurements of k_B2, k_B3, k_B4, and k_B5 all used identical thermometer sleeve enclosures; thus the uncertainty contributions due to thermometer gradient for those four measurements were treated as completely correlated. On the other hand, the thermometers in the measurement of k_B1 did not use the same enclosures as the other four measurements, therefore the uncertainty contribution from thermometer gradient for k_B1 was not correlated with k_B2, k_B3, k_B4 and k_B5. The microwave resonant procedure obviously differs from the two-color interferometry so that their uncertainty entries are not correlated.

The procedure for corrections of the perturbations caused by the viscous and the thermal boundary layers was given in [11, 13]. The same procedure was applied for the determinations of k_B1, k_B2, k_B3, k_B4 and k_B5. Nevertheless, the five determinations were conducted independently in different measurements with the different resonators. Thus, the uncertainty contributions from boundary layer corrections in table 5 were uncorrelated.

Based on the identification of correlated and uncorrelated uncertainties in table 5, we formed the covariance matrix by following the procedure presented in [22, 23]. Gaiser *et al* [30] reported the calculation of the weighted mean of different determinations of k_B considering uncertainty correlations based on the theory given in [22, 23]. For c-AGT, imperfections perturb measurements of the parameters in equation (1) independently. The perturbations, approximated to first order, are

$$k_{\mathrm{B}i} = k_{\mathrm{B}} + \sum_{m=1}^{M} \delta(k_{\mathrm{B}i})_m. \tag{10}$$

In our case, $i = 1, \ldots, 5$ accounts for the five determinations. According to [22, 23], the variance $u(k_{\mathrm{B}i}, k_{\mathrm{B}i})$ is equal to the square of the uncertainty for $k_{\mathrm{B}i}$, i.e. $\mathrm{cov}(k_{\mathrm{B}i}, k_{\mathrm{B}i}) = u^2(k_{\mathrm{B}i})$. The covariances, $\mathrm{cov}(k_{\mathrm{B}i}, k_{\mathrm{B}j})$, which are not zero for the uncertainties of correlation, are

$$\mathrm{cov}\,(k_{\mathrm{B}i}, k_{\mathrm{B}j}) = \sum_{m1,m2}^{M} \mathrm{cov}\left[\delta(k_{\mathrm{B}i})_{m1}, \delta(k_{\mathrm{B}j})_{m2}\right] \tag{11}$$

where $i,j = 1,\ldots,5, M = 7$ (seven sets of uncertainties in table 5). As stated above, the uncertainties in different rows were caused by different perturbation mechanisms so that they were completely uncorrelated. Accordingly, $\mathrm{cov}\left[\delta(k_{\mathrm{B}i})_{m1}, \delta(k_{\mathrm{B}j})_{m2}\right] \neq 0$ for $m1 = m2$ and $\mathrm{cov}\left[\delta(k_{\mathrm{B}i})_{m1}, \delta(k_{\mathrm{B}j})_{m2}\right] = 0$ for $m1 \neq m2$. As stated above, each set consists of several fine uncertainty items. An item corresponds with one row in table 5. Assume the mth set of uncertainty contribution defined by the function of quantities,

$$\delta(k_{\mathrm{B}i})_m = f_m^{k_{\mathrm{B}i}}(x_1, \ldots, x_L). \tag{12}$$

In equation (12), L stands for the number of items in a set of uncertainty. The first order approximation assumption implies that the mth set consists of the perturbations in linear sum analogous to equation (10). Thus, the functions in equation (12) are linear in practice.

$$\mathrm{cov}\left[\delta(k_{\mathrm{B}i})_m, \delta(k_{\mathrm{B}j})_m\right] = \sum_{l=1}^{L} \left(\frac{\partial f_m^{k_{\mathrm{B}i}}}{\partial x_l}\right)\left(\frac{\partial f_m^{k_{\mathrm{B}j}}}{\partial x_l}\right) u\left(x_l^i\right) u\left(x_l^j\right). \tag{13}$$

Because we catalogue each set of uncertainty into the fine items, we can mark an uncertainty entry completely correlated or completely uncorrelated among the five determinations. As a result, the sensitivity factors are equal to 1 for the completely correlated items or zero for the completely uncorrelated items marked in table 5. For each row in table 5, a 5×5 correlation matrix Ω is created. The diagonal element (i, i) of Ω is equal to 1 if the ith determination has an uncertainty entry in that row, otherwise is equal to zero. The off-diagonal element (i, j) of Ω is equal to 1 if the uncertainty entry of the ith determination correlates with the jth determination. For instance, Ω with respect to the row of 'Thermometer calibration' in table 5 is

$$\begin{bmatrix} 1 & 0 & 0 & 0 & 0 \\ 0 & 1 & 1 & 1 & 0 \\ 0 & 1 & 1 & 1 & 0 \\ 0 & 1 & 1 & 1 & 0 \\ 0 & 0 & 0 & 0 & 1 \end{bmatrix}.$$

Based on the correlation matrix, a 5×5 covariance matrix V_{row} for the same row is created by two steps. First, a vector consisting of the five elements of the row is defined, then an intermediate matrix Γ is created by the transposed vector times the vector. Second, matrix V_{row} is accounted for the Hadamard product of Ω and Γ.

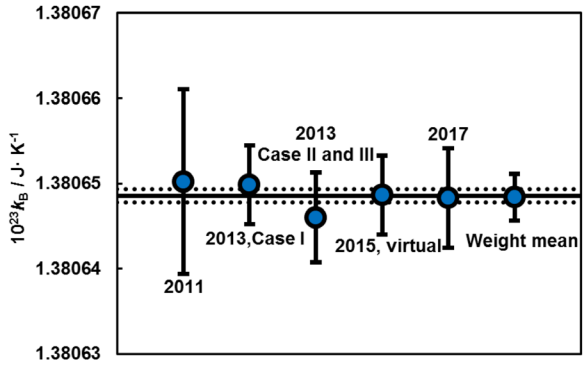

Figure 15. Weighted mean of the k_{B} from c-AGT. The center solid line is the value from CODATA2014 [6] and the dash line is its uncertainty.

The overall covariance matrix V is obtained by summing each matrix V_{row} created on each row in table 5, that is

$$V = \begin{bmatrix} 60.8295 & 0.8002 & 0.8002 & 0.8002 & 0.5334 \\ 0.8002 & 11.1933 & 1.4283 & 1.4283 & 0.6799 \\ 0.8002 & 1.4283 & 14.0438 & 1.4283 & 0.6799 \\ 0.8002 & 1.4283 & 1.4283 & 10.8499 & 0.6799 \\ 0.5334 & 0.6799 & 0.6799 & 0.6799 & 17.7854 \end{bmatrix}.$$

The weight matrix $W = (w_{ij})_{N,N}$ is equal to V^{-1}, where $N = 5$. Given the normalized weights, defined by

$$c_j = \sum_{i=1}^{N} w_{ij} \Big/ \sum_{m,n=1}^{N} w_{mn} \tag{14}$$

the weighted mean $\hat{k}_{\mathrm{B}}$ is given by

$$\hat{k}_{\mathrm{B}} = \sum_{j=1}^{N} k_{\mathrm{B}j} c_j \tag{15}$$

and the standard uncertainty of the weighted mean is

$$u\left(\hat{k}_{\mathrm{B}}\right) = \left(\sum_{m,n=1}^{N} w_{mn}\right)^{-1/2}. \tag{16}$$

The weighted mean $\hat{k}_{\mathrm{B}}$ from the five determinations given in table 5 is $\hat{k}_{\mathrm{B}} = 1.380\,6484(28) \times 10^{-23}$ J K^{-1}. The corresponding gas constant R is equal to 8.314 459(17) J K^{-1} mol^{-1}. The relative standard uncertainty of the weighted mean is $u_{\mathrm{r}}(\hat{k}_{\mathrm{B}}) = 2.0 \times 10^{-6}$, and the relative standard uncertainty of the gas constant is equal to 2.0×10^{-6}. The weighted mean $\hat{k}_{\mathrm{B}}$ with its relative standard uncertainty is illustrated in figure 15.

6. Conclusion

Sections 1–4 of this paper report a new determination of k_{B} with a new cylindrical resonator with the cylindrical shell and the pair of endplates made from OFHC copper. We excited TM microwave resonances to measure the length of the cavity and longitudinal acoustic resonances in argon to measure the speed of sound. The microwave technique to measure the length in the present resonator is the principal difference from

our previous determinations of k_B. The excess half-widths of the acoustic resonances are lower compared with the previous determinations. We attribute the improvement to the fine dimension tolerances and surface finish of the cavity and the endplates obtained by ultra-precise diamond machining. Because the Young's modulus for copper is lower than for bearing steel, the natural vibrations of the copper resonator assembly occur at lower frequencies compared to the resonators made from bearing steel. As before, we used four longitudinal acoustic modes, Al ($l = 2,3,4,5$), for measurements of the speeds of sound in argon at variant pressures.

The new determination of k_B is comparable with the previous determinations using c-AGT despite significant experimental differences. Therefore in section 5 we have included it and the previous four determinations in a globally weighted mean $\hat{\boldsymbol{k}}_B$. Those five determinations shared partial correlations with their measurement uncertainties. We outlined the correlation items in table 5 by referring to [28]. Based on the theory described in reference [22, 23], we formed the covariance matrix of the uncertainty propagation against the lists in table 5. The weighted mean matrix is the inverse of the covariance matrix. Accordingly, the weighted mean $\hat{\boldsymbol{k}}_B$ was estimated to be $1.380\,6484(28) \times 10^{-23}$ J K^{-1} with the relative standard uncertainty of 2.0×10^{-6}. This weighted mean is 0.1×10^{-6} below the k_B given by CODATA2014 [6]. The corresponding gas constant R is equal to 8.314 459(17) J K^{-1} mol^{-1} with the relative standard uncertainty of 2.0×10^{-6}.

Acknowledgments

We acknowledge our appreciations for the machining of the resonator enclosures by Mr Bin Chen and Mr DongFang Wang from Changchun Institute of Optics, Fine Mechanics and Physics, Chinese Academy of Science. This work was supported by the National Key R&D Program of China (no. 2016YFF0200101) and the National Natural Science Foundation of China (nos. 51476153 and 51276175). Feng Xiaojuan thanks the Young Elite Scientist Sponsorship Program (YESS no.2015QNRC001) by CAST for support.

References

[1] Fischer J and Ullrich J 2016 The new system of units 2016 *Nat. Phys.* **12** 4–7
[2] Fischer J 2015 Progress towards a new definition of the kelvin *Metrologia* **52** S364–75
[3] White D R and Fischer J 2015 The Boltzmann constant and the new kelvin *Metrologia* **52** S213–6
[4] de Podesta M 2016 Rethinking the kelvin *Nat. Phys.* **12** 104
[5] Moldover M R, Tew W L and Yoon H W 2016 Advances in thermometry *Nat. Phys.* **12** 7–11
[6] Mohr P J, Newell D B and Taylor B N 2016 CODATA recommended values of the fundamental physical constants: 2014 *Rev. Mod. Phys.* **88** 035009
[7] Moldover M R, Trusler J P M, Edwards T J, Mehl J B and Davis R S 1988 *J. Res. Natl Bur. Stand.* **93** 85–144
[8] de Podesta M, Underwood R J, Sutton G, Morantz P and Harris P 2013 A low-uncertainty measurement of the Boltzmann constant *Metrologia* **50** 354–76
[9] Pitre L, Risegari L, Sparasci F, Plimmer M D, Himbert M E and Giullano Albo P A 2015 Determination of the Boltzmann constant k from the speed of sound in helium gas at the triple point of water *Metrologia* **52** S263–73
[10] Gavioso R M, Ripa D M, Steur P P M, Gaiser C, Truong D, Guianvarc'hv C, Tarizzo P, Stuar F M and Dematteis R A 2015 Determination of the molar gas constant R by acoustic thermometry in helium *Metrologia* **52** S274–304
[11] Lin H, Feng X J, Gillis K A, Moldover M R, Zhang J T, Sun J P and Duan Y Y 2013 Improved determination of the Boltzmann constant using a single, fixed-length cylindrical cavity *Metrologia* **50** 417–32
[12] Gillis K A and Moldover M R 1996 Practical determination of gas densities from the speed of sound using square-well potentials *Int. J. Thermophys.* **17** 1305–24
[13] Zhang J T, Lin H, Feng X J, Sun J P, Gillis K A, Moldover M R and Duan Y Y 2011 Progress toward redetermining the Boltzmann constant with a fixed-path-length cylindrical resonator *Int. J. Thermophys.* **32** 1297–329
[14] Feng X J, Lin H, Gillis K A, Moldover M R and Zhang J T 2015 Test of a virtual cylindrical acoustic resonator for determining the Boltzmann constant *Metrologia* **52** S343–52
[15] Zhang K, Feng X J, Zhang J T, Lin H, Duan Y N and Duan Y Y 2017 Microwave measurements of the length and thermal expansion of a cylindrical resonator for primary acoustic gas thermometry *Meas. Sci. Technol.* **28** 015006
[16] Underwood R J and Edwards G J 20014 Microwave-dimensional measurements of cylindrical resonators for primary acoustic thermometry *Int. J. Thermophys.* **35** 971–84
[17] Ewing M B and Royal D D 2002 A highly-stable cylindrical microwave cavity resonator for the measurement of the relative permittivites of gases *J. Chem. Thermodyn.* **34** 1073
[18] Ewing M B, Mehl J B, Moldover M R and Trusler J P M 1988 Microwave measurements of the thermal expansion of a spherical cavity *Metrologia* **25** 211–9
[19] Underwood R J, Mehl J B, Pitre L, Edwards G, Sutton G and de Podesta M 2010 Waveguide effects on quasi-spherical microwave cavity resonators *Meas. Sci. Technol.* **21** 075103
[20] Underwood R J, Flack D, Morantz P, Sutton G, Shore P and de Podesta M 2011 Dimensional characterization of a quasispherical resonator by microwave and coordinate measurement techniques *Metrologia* **48** 1–15
[21] Moldover M R, Schmidt J W, Gillis K A, Mehl J B and Wright J D 2015 Microwave determination of the volume of a pressure vessel *Meas. Sci. Technol.* **26** 015304
[22] Mohr P J and Taylor B N 1999 CODATA recommended values of the fundamental physical constants: 1998 *J. Phys. Chem. Ref. Data* **28** 1713–852
[23] Mohr P J and Taylor B N 2000 CODATA recommended values of the fundamental physical constants: 1998 *Rev. Mod. Phys.* **72** 351–495
[24] Moldover M R, Gavioso R M, Mehl J B, Pitre L, de Podesta M and Zhang J T 2014 Acoustic Gas thermometry *Metrologia* **51** R1–19
[25] Matula R A 1979 Electrical resistivity of copper, gold, palladium, and silver *J. Phys. Chem. Ref. Data* **8** 1147–298
[26] Yang I, Pitre L, Moldover M R, Zhang J T, Feng X J and Kim J S 2015 Improving acoustic determinations of the Boltzmann constant with mass spectrometer measurements of the molar mass of argon *Metrologia* **52** S394–409

[27] Sharipov F and Moldover M R 2016 Energy accommodation coefficient extracted from acoustic resonator experiments *J.Vac. Sci. Technol.* A **34** 061604
[28] Moldover M R, Gavioso R M and Newell D B 2015 *Metrologia* **52** S376–84
[29] Lee J Y, Marti K, Severinghaus J P, Kawamur K, Yoo H S, Lee J B and Kim J S 2006 *Geochim. Cosmochim. Acta* **70** 4507–12
[30] Gaiser C, Fellmuth B, Haft N, Kuhn A, Thielekrivoi B, Zandt T, Fischer J, Jusko O and Sabuga W 2017 *Metrologia* **54** 280–9